Technical Physics, 2025, Vol. 70, No. 4

06

The spall strength of MPG-8 and I-3 graphites under shock loading up to 2 GPa

© A.S. Savinykh, G.V. Garkushin, S.V. Razorenov, A.N. Zhukov

Federal Research Center for Problems of Chemical Physics and Medical Chemistry, Russian Academy of Sciences,
142432 Chernogolovka, Moscow region, Russia
e-mail: savas@ficp.ac.ru

Received November 7, 2024
Revised December 28, 2024
Accepted January 9, 2024

The spall strength of fine-grained pressed graphite MPG-8 and high-strength isotropic graphite I-3 were measured under shock wave loading with an amplitude not exceeding 2 GPa. Using the VISAR laser Doppler velocimeter, the structure of compression and rarefaction waves in graphite was recorded in experiments. It was found that with an increase in the maximum compression stress, the spall strength of graphite MPG-8 increases significantly, while for graphite I-3 — it does not change. The value of the Hugoniot elastic limit of the studied graphites was measured at 0.5 GPa, and a strong dependence of the velocity of the compaction wave on the maximum compression stress was shown.

Keywords: Graphite, shock waves, deformation, spall strength, Hugoniot.

DOI: 10.61011/TP.2025.04.61213.411-24

Introduction

Graphite is widely used as a structural material in many industry fields and generally represents itself a polycrystalline material, where, along with grain boundaries and stacking faults like twins, a significant number of single faults may be observed. From the very beginning of its development, graphite has been used in nuclear power engineering as a good retarder with a small neutron capture cross-section and as a structural material for fuel element shells and matrices, anti-fragmentation coatings of spherical fuel particles in high-temperature gas reactors, pipelines, etc. [1–5]. Graphite of various grades is used to make some parts of reactor fuel assemblies, and it is used as a matrix and shell material in high-temperature reactors. Thus, taking into account the critical operating conditions in nuclear power plants, graphite has unique physical and chemical properties, high mechanical strength, isotropy, good erosion, corrosion and chemical resistance to radiation exposure, and contains a small amount of impurities. In addition, graphite fabrication technologies ensure a low coefficient of thermal expansion, as well as high thermal and electrical conductivity of the material when exposed to radiation.

One of the most important characteristics of graphite materials is its strength, which can vary significantly depending on the methods of their manufacture, so graphite products with the same density but different grades, differing in structure, may have various strengths. The general rule is that a more finely structured graphite composite has, as a rule, greater strength and a longer service life. The strength of different types of graphite under static loads can vary from 10 to 100 MPa or more, depending on the fabrication method and loading conditions. Under extreme operating conditions, graphite product structures can be subjected to dynamic (shock) loads of varying intensity, however, there is very little data on the strength behavior of graphite under pulsed conditions. In [6], a graphite spall test was performed to study its dynamic behavior under tension using Hopkinson bars at a deformation rate of $5 \cdot 10^3\,\mathrm{s}^{-1}$. Studies of the fragmentation of graphite samples during their collision with a small impactor at velocities of up to 5 km/s [7] were carried out. Basically, measurements of critical tensile stresses under spall conditions were carried out under high-power laser exposure of nanosecond duration [8–11], when wave profiles were recorded during loading, and the graphite spall strength was estimated equal to ~ 135 MPa in these conditions. The spall strength of graphite calculated in [9] at maximal possible deformation rate of $1.4 \cdot 10^7\,\mathrm{s}^{-1}$ amounted to 2.1 GPa, which makes 64 % of graphite theoretical ultimate strength.

In this paper, measurements of spall strength, Hugoniot elastic limit, and wave velocity of graphite seals MPG-8 and I-3 have been carried out, which are necessary to predict their strength behavior under intense artificial exposure, natural impacts or terrorist attacks.

1. Studied materials and experimental methods

Two types of graphite samples were examined. Graphite of grade MPG-8 — a high-strength type of artificial graphite obtained by cold pressing of graphite powder from the low-ash petroleum coke, — has high mechanical strength due to its fine-grained structure. Retains its mechanical and thermodynamic properties up to temperatures above 2000 °C. Graphite of grade I-3 is an isotropic, high-

Table 1. Structural parameters of graphite MPG-8 and I-3 defined during analysis

Structural parameter of graphite	MPG-8	I-3
Parameter of the crystal lattice$a$, Å	2.4635(2)	2.4634(2)
Parameter of the crystal lattice$c$, Å	6.754(1)	6.768(1)
X-ray density ρ, g/cm^3	2.247	2.243
Coefficient of predominant orientation R	1.05	1.03
Degree of a 3D regularity P_3	0.48	0.41
Degree of a 3D regularity P_3^*	0.59	0.47
Concentration of the poly-type deformational faults α	0.11	0.03
Concentration of the poly-type growth faults σ	0.19	0.10
Concentration of turbo-strata faults γ	0.41	0.53

strength fine-grained structural graphite obtained by isostatic pressing, where the properties of blanks and products are not impacted by the direction of acting loads; this graphite is distinguished by high wear resistance and thermal conductivity.

A characteristic feature of artificial graphite materials is the presence of developed porosity in them, which is related to their fabrication technology and the properties of coke fillers. The operational properties and behavior of graphite materials under various conditions are greatly dependent on the porous structure and sizes of pores. The total porosity of the samples studied in this paper was determined by the formula

$$\Pi = \left(1 - \frac{\rho_{sample}}{\rho_{theor}}\right) \cdot 100\,\%$$

where ρ_{sample} — density of the studied sample, ρ_{theor} — theoretical density of material. When calculating porosity, the density of nonporous graphite was used which was $\rho_0 = 2.265\,\mathrm{g/cm^3}$.

During samples preparation process the axial c_l and shear c_s velocities of sound were measured using a device for acoustic waves propagation rate measurements (MGNIVP „Akustika"). The density of the studied samples ρ_{00} was determined by hydrostatic weighing using analytical scales ME204T („Mettler Toledo") in automatic mode.

The graphite samples were examined in detail by methods of powder X-ray diffraction. X-ray images were taken using DRON-4 diffractometer in Bragg-Brentano geometry. The surface of the samples exposed to X-rays was pre-leveled and cleaned by machine turning. CuKα radiation, Ni-filter was used. The diffraction patterns were recorded in the range of 2θ $10^\circ - 165^\circ$ step by step. The step is 0.05°, detection time at every step is 4 s. X-ray images were analyzed by various methods. The coefficient of predominant orientation R (March Dollase model), the crystal lattice parameters a, c and the X-ray density ρ calculated on their basis were determined using GSAS software package [12]. The broadening of peaks on X-ray images and its possible causes were investigated using construction of Williamson-Hall diagrams [13]. The study suggests a sufficiently large size of coherent scattering regions (the size of crystallites), both along the it a axis and c axis (at least more than 50 nm), a low level of distortion of graphite grids, but also significant micro-distortions perpendicular to them (along c axis) and a noticeable concentration of turbo-strata and polytypic stacking faults. Concentration of turbo-strata faults (γ), polytypic growth (δ) and deformational (α) faults, as well as degree of a 3D regularity P_3 and P_3^* were calculated by formulae from [14]. The 3D regularity P_3 was calculated based on the lattice parameter c, and P_3^* was defined based on the narrowing of line 112. The structural parameters of MPG-8 and I-3 graphite calculated during X-ray examination are shown in Table 1.

What stands out is the coefficient of predominant orientation R, which is close to unity, which is consistent with the poorly grain-oriented graphite products. A coefficient equal to unity indicates the absence of texture [12]. The analysis allows us to conclude that the samples MPG-8 and I-3 are moderately crystallized hexagonal graphite materials with a noticeable concentration of turbo-strata and polytypic faults with a very low level of grain-oriented texture, especially for graphite I-3.

The structure of the graphite samples under study was preliminarily examined using OLYMPUS GX53 inverter metallurgical microscope. Figure 1 shows photo of the surface structure of the studied graphite at 10× magnification. As can be seen in Fig. 1, a, fine-grained graphite MPG 8 has a fairly homogeneous structure distinguished by a significant number of pores, mainly round and oval in cross-section. The pores are mainly — up to 25 μm in size, pores with sizes from 25 to 40 μm are also observed and the pores with sizes from 40 to 60 μm are also present in small amount. The fine-grained isostatic graphite I-3 (ISEM-3) is also featuring a quite homogeneous structure.

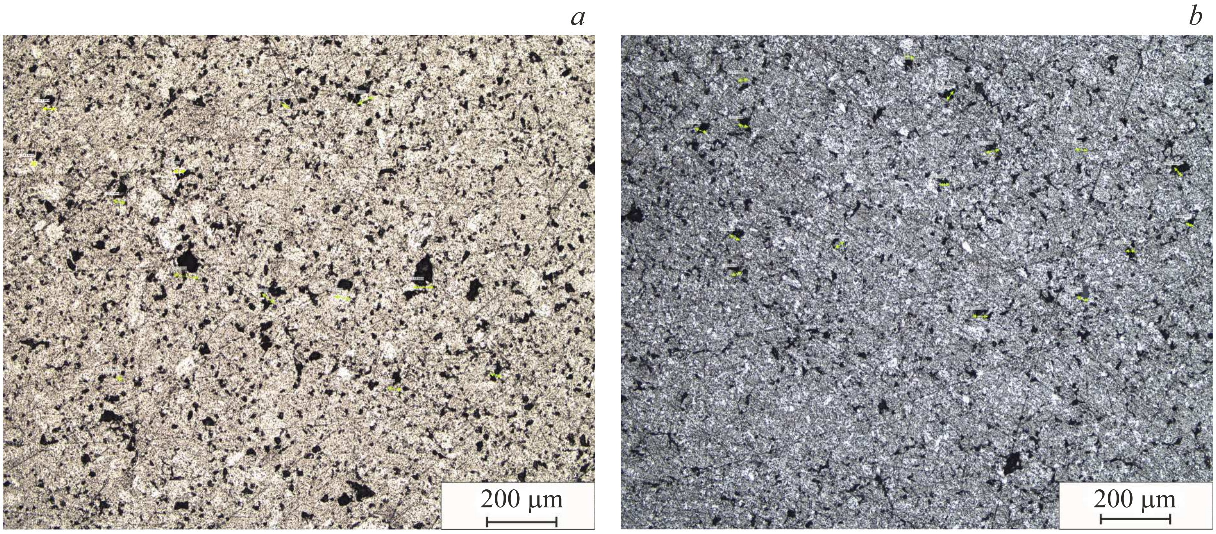

Figure 1. Microstructures of graphite during increase 10×; *a* — MPG-8, *b* — I-3.

Fig. 1, *b* shows that geometry of pores differs from the fine-grained graphite MPG-8. The pores are less in size, their shape — is predominantly elongated, longitudinal, 30 to 90 μm in length. Most of the relatively round pores are no more than 20 μm in size. The pores 20 to 40 μm in size are relatively rare, and large pores up to 50 μm in size are in small amount. Thus, graphite structure studied in microscope has shown that the macroscopic porosity of the samples directly depends on the pore size. Table 2 gives the mechanical properties of the structural graphite studied in this paper.

The 5 mm thick plates were used as initial graphite blanks. For shock-wave experiments, plane-parallel rectangular samples with a size of 30 × 30 mm were cut out of graphite plates on ART 120 electric spark machine. Such ratio of the samples' thickness and linear dimensions made it possible to keep the deformation process unidimensional in planar collision during the time required to detect the full wave profiles. The surfaces of the flat graphite samples were preliminary machined using 2500-grain size sanding paper and alcohol to a mirror-like gloss while maintaining plane-parallel sides. To ensure the reflection of probing laser radiation when registering the surface velocity with a laser interferometer, the aluminum layer $(1-2\,\mu\text{m})$ was sputtered on one of the surfaces using a vacuum systemVUP-2.

The shock-wave loading of the graphite samples was carried out using a pneumatic gun PP-50, that allowed to accelerate the copper (Cu) impactor 2 mm thick to the velocities of (230 ± 10), (350 ± 10), (440 ± 10) and (520 ± 10) m/s prior to collision with the sample. The flat impactors were located at the end of a hollow aluminum projectile, which was accelerated in the gun by compressed air or helium, providing a flat impact with the sample. In every experiment the velocity of the impactor and its slant were measured by two pairs of electric contact sensors. The gun barrel and the receiving chamber, where the sample was located, were pumped out prior to the experiment. All experiments were performed at room temperature. In all experiments the free surface velocities of the studied samples (full wave profiles $u_{fs}(t)$) were recorded using laser Doppler interferometric velocity meter VISAR [15], having temporal resolution of ~ 1 ns and spatial resolution of ~ 0.1 mm.

Table 2. Mechanical properties of MPG-8 and I-3 graphite materials.

Characteristic of	MPG-8	I-3
Measured density ρ_{00}, g/cm^3	1.89	1.91
Measured porosity, %	17	16
Axial sound velocity c_l, m/s	2797	2627
Shear sound velocity c_s, m/s	1559	1586
Ash-content, %, no more than	0.005	0.00005
Grain size, μm	8–10	8–10
Modulus of elasticity, GPa	11	11
Ultimate bending strength, MPa, not less than	50	55–58
Ultimate compression strength, MPa, not less than	90	90

2. Finding the impact compression of the studied graphite materials

Figure 2 shows the results of recording the free surface velocity profiles in shock wave experiments with the studied graphite samples — fine-grained pressed (MPG-8)

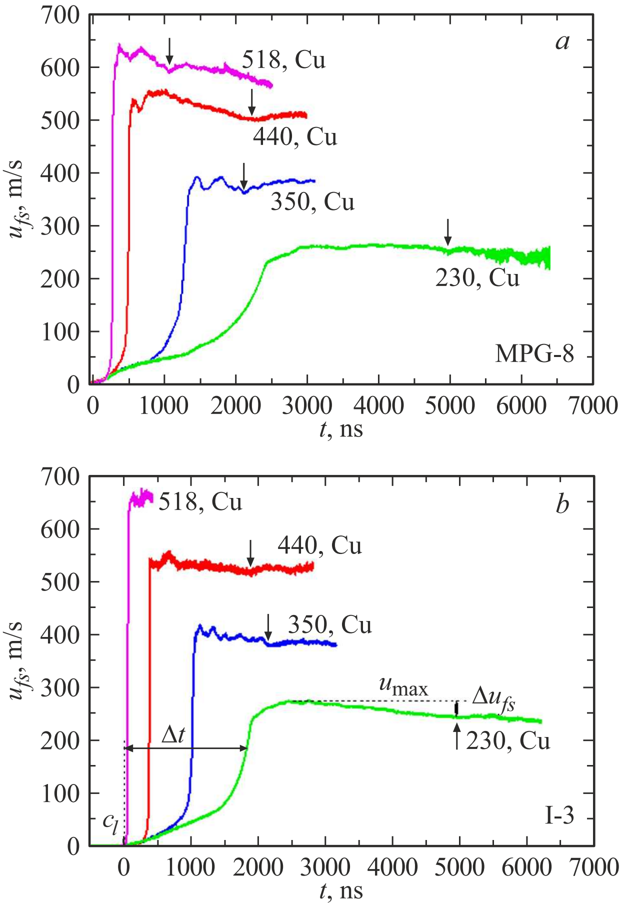

Figure 2. Free surface velocity profiles of graphite samples MPG-8 and I-3 which are 5 mm thick. Velocity (m/s) and the material of the impactor are indicated for the profiles, the arrows show the time points of the spall fracture.

and isostatic I-3 graphite samples obtained at impactor velocities of 230, 350, 440 and 520 m/s. On all wave profiles, the output of an elastic wave to the surface is sequentially detected, with the wave amplitude decreasing with the rise of maximum compression stress. Then goes a compression wave and a region of parameter constancy following it, which, in turn, is followed by a rarefaction wave associated with the dynamic stretching of the material and its subsequent destruction. The parameter constancy duration is defined by the wave reverberation time in the impactor.

Figure 3 shows the frontal parts of the compression waves of the studied graphite materials upon impact with a 2 mm thick copper impactor at a velocity of 230 m/s. The output of elastic wave and further output of compression wave are recorded on the profiles. The shape of the elastic wave depends on the total volume of the pores, their sizes and configurations, and the uniformity of the pore volume distribution for each examined graphite material. Graphite I-3 demonstrates a smooth increase in the free surface velocity from zero to the output of the compression wave, with the difference that the rise of the free surface velocity in the compression wave is steeper than that of graphite MPG-8. Measuring the propagation velocity of the first compression wave using electric contact sensors showed that the first compression wave propagates at the longitudinal velocity of sound. Figure 3 shows how the free surface velocities u_{HEL} of the studied graphite materials were determined, at which the elastic compression of the material under study ends and the compression wave or compaction begins to form. Based on the measured free surface velocity u_{HEL}, the compression stress corresponding to the dynamic elastic limit of the examined material was estimated using the relation $\sigma_{HEL} = 1/2\rho_{00}c_l u_{HEL}$. Thus, for graphite MPG-8 $\sigma_{HEL} = 196$ MPa, for I-3 $\sigma_{HEL} = 195$ MPa. The obtained values of the dynamic elastic limit for each graphite are twice as high as the compressive strength measured under static loading conditions (Table 2).

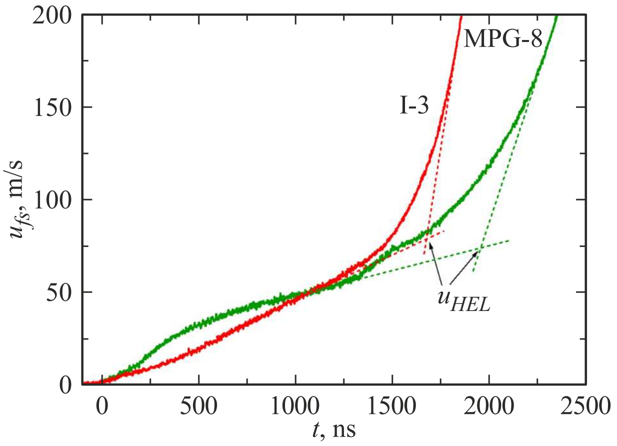

Figure 3. Frontal portions of compression waves of MPG-8 and I-3 graphite materials with a thickness of 5 mm hit by a 2 mm copper plate with a velocity of 230 m/s.

Shock compression of a porous substance leads to its thermal heating [16]. Since in this work maximum compression pressure does not exceed 2 GPa, in order to calculate the shock wave velocity and mass velocity of porous graphite, it was assumed that during shock compression of the porous substance, all the pores are „closed“, and the examined substance becomes nonporous. In weak shock waves, the heating of a porous substance is negligible. To calculate the specific volume of a shock-compressed substance let's use the relation $V = V_0\frac{U_s - u_p}{U_s}$, where V_0 — specific volume of solid substance $V_0 = 1/\rho_0$ (ρ_0 — density of solid graphite equal to 2.265 g/cm^3), U_S — velocity of the shock wave in a solid substance, u_p — mass velocity of solid substance. Pressure P in solid substance is found using the relation $P = \rho_0 U_S u_p$. The dependence of U_S on mass velocity u_p of solid graphite was obtained by approximation of experimental data [17,18] to the level of phase transformation pressure as illustrated in Fig. 4, through the relation $U_S = 3.95 + 2.03u_p$. To evaluate the shock wave velocity U_{S1} and mass velocity u_{p1} of porous graphite let's use the relations $U_{S1} = \sqrt{p\,\frac{V_{00}^2}{V_{00}-V}}$ and $u_{p1} = \frac{P}{\rho_{00}U_{S1}}$, where $V_{00} = \frac{1}{\rho_{00}}$ (ρ_{00} — measured density of porous graphite). The evaluation was made as follows. Since the porous substance becomes non-porous or has negligible porosity during impact loading, and heating of the porous substance during impact compression is neglected, the specific volume V and pressure P are calculated in a solid substance over the entire range of mass velocities of the solid substance. Then, shock wave velocities U_{S1} and mass velocities u_{p1} occurring in a porous substance under pressure P and specific volume V are calculated.

Figure 4 shows the calculated dependences of the shock wave velocity on the mass velocity for the studied porous graphite. The calculated dependences of porous graphite in coordinates $U_S - u_p$ are significantly nonlinear and lie lower than the dependence for solid (pyrolytic) graphite [17,18]. Also the data for reactor porous graphite are given there [18]. Fig. 4 shows experimental data on the compression wave velocity versus mass velocity obtained in this work for the studied graphite materials. The analysis of mass velocity u_{p1} is schematically shown in Fig. 5. With the help of electrical contact sensors, it was experimentally determined that the output of the first wave to a free surface occurs at the axial velocity of sound cl; to calculate the velocity of the compression wave, we use the ratio $U_{S1} = c_l\,\frac{h_s/c_l-\Delta t/2}{h_s/c_l+\Delta t/2}$, where h_s — sample thickness, Δt — difference between the output of elastic wave and compression wave to a free surface, as shown in Fig. 2. The obtained values of maximum free surface velocity $u_{\max}$ and compression wave velocity U_{S1} for the studied graphite are also presented in Table 3. The figure shows good consistency of the calculated dependences of mass velocity on shock wave velocity compared to the experimentally obtained data.

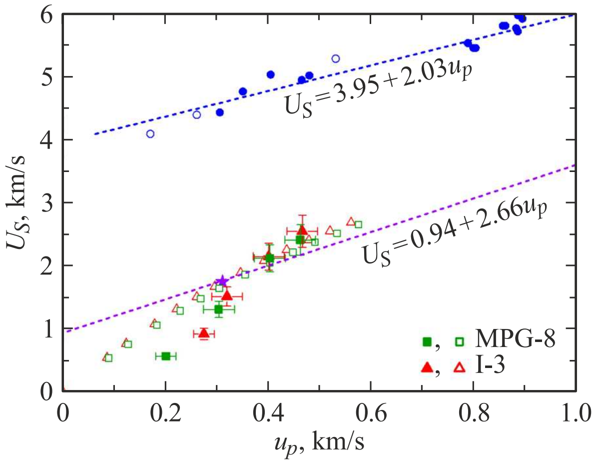

Figure 4. Shock adiabats of porous and solid graphite materials in coordinates of „mass velocity — shock wave velocities". Empty square and triangle — analysis, full square and triangle — experiment, full circle — pyrolytic graphite [17], empty circle — pyrolytic graphite [18], star-porous reactor graphite [18].

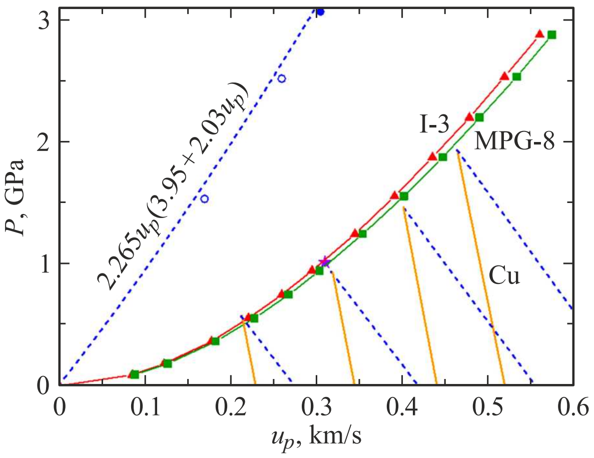

Figure 5. Shock adiabats of porous and solid graphite materials in coordinates of „mass velocity — pressure". Square and triangle — analysis, full circle — pyrolytic graphite [17], empty circle — pyrolytic graphite [18], star-reactor graphite [18].

Using the calculated values of the mass velocity u_{p1} for a porous substance and the corresponding pressure for a solid substance, the shock adiabats of the porous substance were constructed in pressure-mass velocity coordinates, shown in Fig.5. In both, $U_S - u_p$ coordinates and $P - u_p$ coordinates, the calculated impact adiabats for porous graphite are lower than for solid graphite. Figure 5 also shows specularly reflected copper adiabatic lines constructed from velocity values that coincide with the velocities of the impactors, and specularly reflected adiabatic lines of solid graphite plotted based on experimentally determined values of the maximum velocity of free surface umax. At the intersection of a specularly reflected copper adiabat with a specularly reflected adiabat of solid graphite, the mass velocity u_{pl} in graphite was determined, since the discharge of compacted graphite occurs along the adiabatic line of solid material. The maximum compression stresses in each experiment were calculated using ratio $\sigma_{\max} = \sigma_{HEL} + \rho_{el}U_s(u_{pl} - u_{HEL}/2)$ [19], where $\rho_{el} = \rho_0 c_l/(c_l - u_{HEL}/2)$ is the density after elastic compression. The values of the mass velocity u_{pl} and maximum compression stress $\sigma_{\max}$ determined in this way are summarized in Table 3.

Figure 6 shows the compression wave velocities calculated from the measured profiles U_{S1} depending on the maximum compression stress $\sigma_{\max}$ of the studied graphite materials. It can be seen that as the maximum compression stress rises, the recorded compression wave velocities grow uniformly while maintaining a two-wave structure on the free surface velocity profile. The two-wave structure on $u_{fs}(t)$ profiles of the examined graphite materials will be preserved until the compression wave velocity reaches the sound longitudinal velocity.

Table 3. Setup and results of experiments with graphite I-3 and MPG-8

№	h_s, mm	V_{imp}, m/s	h_{imp}, mm / material	Δt, ns	U_{S1}, km/s	Δu_{fs}, m/s	σ_{sp}, MPa	$u_{\max}$, m/s	u_{pl}, m/s	$\sigma_{\max}$, GPa
I-3										
1	4.981	520	1.996 / Cu	62	2.54	–	–	662	465	2.22
2	4.953	440	1.969 / Cu	383	2.14	30	134	553	400	1.65
3	4.975	350	1.983 / Cu	1023	1.51	32	143	418	319	0.99
4	4.958	230	1.983 / Cu	1819	0.92	30	134	274	212	0.51
MPG-8										
5	4.950	520	1.980 / Cu	268	2.40	44	196	634	461	2.10
6	4.927	440	1.983 / Cu	490	2.12	52	233	551	402	1.64
7	4.948	350	1.988 / Cu	1286	1.31	23	103	389	303	0.84
8	4.936	230	1.990 / Cu	2344	0.57	10	45	259	213	0.39

Note: h_s — sample thickness, V_{imp} — impactor velocity, h_{imp} — impactor thickness, Δt — time difference between elastic wave output and sealing wave, U_{S1} — sealing wave velocity, Δu_{fs} — spall pulse amplitude, σ_{sp} — spall strength, $u_{\max}$ — maximum free surface velocity, u_{pl} — mass velocity, $\sigma_{\max}$ — maximum compression stress.

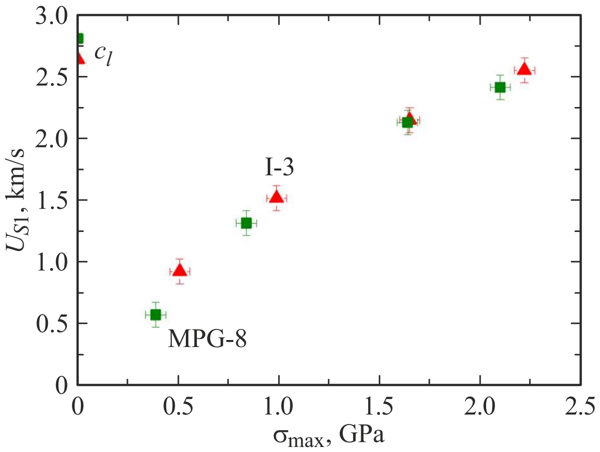

Figure 6. Compression wave velocity versus maximum compression stress of graphite I-3 and MPG-8. The measured values of axial sound velocity are given.

3. Results of measurement of graphite spall strength MPG-8 and I-3

Dynamic strength of materials in the extremely low load time region is analyzed by examining the so-called „spall" events when compression pulses are reflected from free surfaces of the body [20]. High-velocity spall fracture is a kinetic process of initiation, growth and merging of multiple discontinuities. When the expansion wave coming from the rear side of the impactor interacts with the expansion wave reflected from the free surface of the sample, inside of it tensile stresses are generated, and when they exceed the value critical for this material, a damage, i.e. spall is initiated in the sample. In this case, the relaxation of tensile stresses occurs and a compression wave (spall pulse) is formed, the output of which to the sample surface usually causes a second rise in its velocity — a compression wave, the so called „spall pulse". The decrement of the surface velocity Δu_{fs} at its decline from the maximum to the value before the front of the spall pulse is proportional to the magnitude of the destructive stress — the spall strength of the material under these loading conditions. In the acoustic approximation the spall strength of the material is calculated using ratio [21]:

$$\sigma_{sp} = \frac{1}{2}\rho_0 c_b \Delta u_{fs}. \qquad (1)$$

The destruction of materials such as graphite occurs along the volume of the sample and the boundaries of crystals and their conglomerates. Reducing their size leads to more complex and difficult crack propagation due to the greater number of obstacles and thus results in high strength of fine-grained graphite samplesMPG-8 and I-3.

The spall fracture, recorded on the velocity profiles of the free surface and shown by the arrows in Fig. 2, occurred already in the compacted graphite. Spall strength was calculated using relation (1), where ρ_0 — density of solid graphite, equal to 2.265 g/cm^3, $c_b = 3.95$ km/s — volumetric velocity of solid graphite taken from approximation of data for solid graphite Fig. 4. The measured values Δu_{fs} and defined values σ_{sp} were summarized in Table 3. As shown by the analysis of the obtained wave profiles (Fig. 2), for graphite MPG-8, there is a tendency for the value of Δu_{fs} to increase with growth of shock compression pressure. Fig. 7 shows the spall strength versus maximal compression strength. With an increase in the maximum compression stress, a significant growth of spall strength of graphite MPG-8 is observed. In graphite I-3, with the rise of

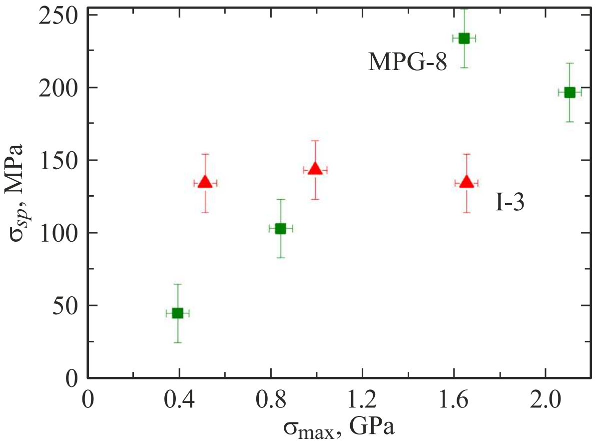

Figure 7. Spall strength versus maximal compression stress of graphite MPG-8 and I-3.

maximum compression stress, the tensile strength remains at the same level. Experiments have shown a significant variation in the strength of the studied graphite materials. In these graphite materials, their strength properties depend on their dispersion, supramolecular and crystalline structures, which, as experiments have shown, are insensitive to the compression intensity in this pressure range.

Conclusion

The wave profiles of the reactor graphite samples MPG-8 and I-3 under shock-wave loading of 2 GPa were measured using Doppler interferometer VISAR. The maximum compression stresses in experiments with shock-wave loading were determined. The studied graphite materials demonstrate the inverse dependence of the elastic wave amplitude on the maximum compression stress. It is shown that the velocity of an elastic wave propagates together with the axial velocity of sound. There is a strong dependence of the compression wave velocity on maximum compression stress to a value of velocity not higher than the axial velocity of sound. Hugoniot elastic limits for graphite samples 5 mm thick were determined. The highest values σ_{HEL} are registered at $\sigma_{\max} \sim 0.5$ GPa and for MPG-8 graphite make 196 MPa, while for I-3 graph— 195 MPa. From the analysis of the wave profiles, the spall strength of the studied graphite samples in the range of deformation rates $\sim 10^3 - 10^4\,\mathrm{s}^{-1}$ before fracture were determined. With an increase in the maximum compression stress to 2 the GPa the spall strength of graphite MPG-8 increases from 50 to 230 MPa, while that of graphite I-3 practically does not change and lies in the range of 110−140 MPa.

Funding

The work was done under the Contract № 1770641334821000138 0/22398/89 of 23 May 2023 and State Assignment of the Russian Ministry of Science „Complex research of physical and chemical properties and processes in the substance under conditions of high energy exposures“, registration № 124020600049-8.

Conflict of interest

The authors declare that they have no conflict of interest.

References

[1] S.E. Vyatkin, A.N. Deev, V.G. Nagorny, V.S. Ostrovsky, A.M. Sigarev, T.A. Sokker. *Yaderny grafit* (Atomizdat, M., 1967) (in Russian).

[2] E.I. Zhmurikov, I.A. Bubnenkov, V.V. Dremov, S.I. Samarin, A.S. Pokrovsky, D.V. Kharkov. *Grafir v nauke i yadernoy tekhnike* (Novosibirsk, 2013) (in Russian).

[3] Y.S. Virgilyev, A.N. Seleznev, A.A. Sviridov, I.P. Kalyagina. Russian Chemical Journal, **50** (1), 4 (2006).

[4] A.V. Bushuev, A.F. Kozhin, E.V. Petrova, V.N. Zubarev, T.B. Alieva, N.A. Girke. *Radioaktivny reaktorny grafit* (NIYaU MIFI, M., 2015) (in Russian).

[5] *Graphite properties and characteristics for industrial applications* (Entegris Poco Materials, Texas, 2015)

[6] L. Peroni, M. Scapin, F. Carra, N. Mariani. Key Eng. Mater., **569−570**, 103 (2013). DOI: 10.4028/www.scientific.net/KEM.569-570.103

[7] D. Hébert, G. Seisson, J.-L. Ruller, I. Bertron, L. Hallo, J.-M. Chevalier, C. Thessieux, F. Guillet, M. Boustie, L. Berthe. Philos. Trans. R Soc. London, Ser. A, **375**, 2085 (2017).

[8] G. Seisson, G. Prudhomme, P.-A. Frugier, D. Hébert, E. Lescoute, A. Sollier, L. Videau, P. Mercier, M. Boustie, L. Berthe. Int. J. Impact. Eng., **91**, 68 (2016). DOI: 10.1016/j.ijimpeng.2015.12.012

[9] R.S. Belikov, I.K. Krasyuk, T. Rienecker, A.Yu. Semenov, O.N. Rosmej, I.A. Stuchebryukhov, M. Tomut, K.V. Khishchenko, A. Schoenle. Quant. Electron., **45** (5), 421 (2015). DOI: 10.1070/QE2015v045n05ABEH015759

[10] A. Morena, L. Peroni. Materials, **14**, 7079 (2021). DOI: 10.3390/ma14227079

[11] G. Seisson, D. Hébert, I. Bertron, L. Videau, P. Combis, L. Berthe, M. Boustie. J. Phys. Conf. Ser., **500**, 112057 (2014). DOI: 10.1088/1742-6596/500/11/112057

[12] A.C. Larson, R.B. Von Dreele. *General structure analysis system* (GSAS) (Los Alamos National Laboratory Report, LAUR 86−748, 2004)

[13] S.V. Tsybulya, S.V. Cherepanova. *Vvedenie v strukturny analys nanokristallov*. training guide (NGU, Novosibirks, 2008) (in Russian).

[14] A.V. Kurdyumov, V.F. Britun, N.K. Borimerchuk, V.V. Yarosh. *Martensitnyye i diffuzionnyye prevrashcheniya v uglerode i nitride bora pri udarnom szhatii* (Kupriyanova, Kiyev, 2005) (in Russian).

[15] L.M. Barker, R.E. Hollenbach. J. Appl. Phys., **43**, 4669 (1972). DOI: 10.1063/1.1660986

[16] Ya.B. Zel'dovich, Yu.P. Raizer, *Fizika udarnykh voln i vysokotemperaturnykh gidrodinamicheskikh yavlenii* (Fizmatlit, M., 2008), (in Russian).

[17] N.L. Coleburn. J. Chem. Phys., **40**, 71 (1964). DOI: 10.1063/1.1724896

[18] R.F. Trunin, L.F. Gudarenko, M.V. Zhernokletov, G.V. Simakov, *Eksperimental'nye dannye po udarno-volnovomu szhatiyu i adiabaticheskomu rasshireniyu kondensirovannykh veshchestv* (RFYaTs–VNIIEF, Sarov, 2006) (in Russian).

[19] E.B. Zaretsky, G.I. Kanel. J. Appl. Phys., **117**, 195901 (2015). DOI: 10.1063/1.4921356

[20] T. Antoun, L. Seaman, D.R. Curran, G.I. Kanel, S.V. Razorenov, A.V. Utkin. *Spall Fracture* (Springer, 2003)

[21] G.I. Kanel. Intern. J. Fracture, **163** (1–2), 173 (2010). DOI: 10.1007/s10704-009-9438-0

Translated by EgoTranslating